Lattice thermal conductivity of Bi₂Te₃ and SnSe using Debye-Callaway and Monte Carlo phonon transport modeling: Application to nanofilms and nanowires

Patricia Al-Alam, Gilles Pernot, Mykola Isaiev, and David Lacroix [*]
Université de Lorraine, CNRS, LEMTA, Nancy F-54500, France

Melanie De Vos and Nicolas Stein[†]
Université de Lorraine, CNRS, IJL, Nancy F-54500, France

David Osenberg and Laetitia Philippe[‡]
Empa - Swiss Federal Laboratories for Materials Science and Technology, Laboratory for Mechanics of Materials and Nanostructures, CH-3602 Thun, Switzerland

The present work addresses the problem of thermal conductivity simulation in Bi₂Te₃ and SnSe thermoelectric nanostructures. It first details phonon lifetime calculation in both thermoelectric compounds assuming polynomial dispersion properties and the Debye-Callaway model for the relaxation-time approximation. For both materials, distinct crystallographic directions are considered, i.e., Γ-Z (trigonal axis) and Γ-X (basal plane) for Bi₂Te₃ and Γ-X (a axis), Γ-Y (b axis), and Γ-Z (c axis) for SnSe. On this basis, the lifetime model is parametrized and bulk thermal conductivity is computed through the resolution of the phonon Boltzmann transport equation with a Monte Carlo method. Grüneisen parameter and mass-disorder lifetime are adjusted to fit experimental temperature dependence. The second part of the study addresses the calculation of thermal conductivity for these two thermoelectric materials in the case of thin films (cross-plane case) and nanowires. The main goals of this work are to provide a fully parametric description of heat transport in Bi₂Te₃ and SnSe nanofilms and nanowires showing reliable behavior on an extended size range, from 20 nm to 2 μm, and large temperature range (100–500 K for Bi₂Te₃; 200–800 K for SnSe). Comparisons to bulk thermal conductivity calculations and measurements as well as to recent investigations on nanowires, demonstrate the effectiveness of the proposed methodology to deal with nanostructured Bi₂Te₃ and SnSe.

I. INTRODUCTION

Thermoelectric (TE) materials have attracted a significant attention in the past decade in the development of alternative renewable energy devices and more specifically for wasted heat energy harvesting. Such interest was mainly due to the enhancement of the conversion efficiency characterized by the figure of merit ZT which is proportional to the power factor ($S^2\sigma$) to the thermal conductivity (k) ratio. In several works increasing ZT in TE devices was related to nanostructuration of materials as it usually decreases the lattice thermal conductivity [1]. This was demonstrated for well-known TE materials such as those based on Bi₂Te₃ [2,3] and for a broad variety of semiconductors in which the bulk lattice thermal conductivity was found to be drastically reduced when elaborating structurelike superlattices, nanowires, nanofilms, nanoporous, etc. [4]. Both theoretical and experimental studies were carried out in this field with similar conclusions as detailed in review papers on this nanoscale thermal transport topic [5,6]. In this framework theoretical prediction of thermal conductivity of

TE material is a critical issue to find new compounds or to optimize their structuration. Concerning the first issue, recent work by Seko *et al.* [7] had shown that a "machine learning" approach based on a density functional theory (DFT) training set could help in finding new TE materials. In what concerns TE material properties improvement, numerical simulations also provide interesting insights. For instance, in the case of Bi₂Te₃ DFT was used to describe electron and phonon transport [8,9]. The latter work details the contribution of phonon modes to the thermal and electrical conductivities. Furthermore, other techniques such as molecular dynamics (MD) were used to achieve TE atomistic description in bulk [10–12] and nanostructures [13–15]. They show good agreement when comparing to available experimental data. However, in both cases, the required computing resources are large and thus restrict calculations to bulk (where boundary conditions are periodic) or to very small nanostructures for which the number of atoms can be handled with MD. Thus, both DFT and MD methods cannot easily address present nano and micro TE structures which are of interest for applied engineering. In this framework, modeling needs to be simplified to some extent in order to ensure that the used physics still capture the nanoscale interaction of energy carriers. Such approach is possible with kinetic theory based models for phonon transport. The latter relies on the knowledge of phonon lifetime or mean free path

---

[*]david.lacroix@univ-lorraine.fr
[†]nicolas.stein@univ-lorraine.fr
[‡]Laetitia.Philippe@empa.ch

(MFP) and can be expressed as the sum $k = 1/3 \Sigma C_i v_i^2 \tau_i$ with C the heat capacity, v the velocity, and τ the lifetime of energy carriers. This model has been extensively used to investigate thermal transport in semiconductors and physical description of phonon interactions are well known for basic compounds such as silicon and germanium. Seminal studies by Callaway [16], Holland [17], and Glassbrenner and Slack [18] had given a simple formalism assuming isotropic dispersion properties in materials and the relaxation-time approximation in the solution of the Boltzmann transport equation (BTE). This kind of modeling has proven to be accurate on an extended range of temperatures and for several kinds of materials. Yet, it relies on a semiempirical description of lifetime parameters for each considered phonon scattering mechanism and thus needs to be compared to experimental data in order to fit the unknown parameters. This adjustment procedure must be done from low to high temperatures as scattering mechanisms that dominate phonon transport change with the temperature level.

Apart from well-known semiconductors (Si, Ge, etc.), the latter method was scarcely used for usual TE compounds like Bi_2Te_3. During past years, some attempts have been made to circumvent these limitations, using kinetic models that take into account the dispersion properties of Bi_2Te_3 and phonon mean free paths [19] or lifetimes with the latter quantities being evaluated by different techniques like time domain normal mode analysis [20] or semianalytic formula [21,22]. For SnSe, there is even less literature on phonon transport properties which can be directly used in kinetic modeling. Recent studies dealing with SnSe transport property simulations are based on *ab initio* calculations. Among them, some were addressing the structural parameters of SnSe compounds [23] while others had computed thermal conductivity [24–28]. In the latter studies, there are some discrepancies between computed thermal conductivity (TC) values along the three main axes. In addition, comparison to available experimental data is also a source of uncertainties due to the broad dispersion of measured values [23,29–31].

This work focuses on Bi_2Te_3 and SnSe semiconductors, which are both layered compounds. If Bi_2Te_3 is a well established thermoelectric material, SnSe has recently generated a great interest for its law of thermal conductivity. In the present study, we use a lifetime-based approach (semianalytic modeling of phonon scattering) and acoustic dispersion property of phonons along the main crystalline axis of Bi_2Te_3 and SnSe to recover thermal conductivity of bulk compounds as a function of temperature. Cross-plane thermal conductivity calculation of thick TE materials ($L_z = 1 \mu m$) have been achieved solving the BTE with a Monte Carlo (MC) technique. Comparisons to experimental data and DFT or MD calculation allow us to adjust unknown parameters of the model. Then, in a second part of this work we have taken advantage of the MC method to deal with several types of nanostructuration to investigate size effect occurring in thin films and nanowires. The paper is organized as follows: (i) phonon frequencies and lifetime properties of both TE compounds of interest are described in the frame of polynomial dispersion curve assumption; (ii) details regarding the numerical method used to solve phonon transport in the considered nanostructures are given; (iii) thermal conductivity of Bi_2Te_3 and SnSe as a function of T

are detailed and compared to the literature; and iv) cross-plane TC of thin films with decreasing thickness is then considered; similar calculations are also achieved for nanowires with several lengths. All size-dependent calculations are compared to available existing experimental data.

II. PHONON DISPERSION PROPERTIES OF Bi_2Te_3 AND SnSe

Inputs for thermal conductivity modeling using a kinetic approach or BTE resolution in the frame of the relaxation-time approximation implies that one knows the group velocity of energy carriers for each phonon mode as well as the scattering lifetimes related to these modes. In the present work, for each main crystalline direction (of interest) in both TE compounds we assume (i) that only acoustic modes contribute to thermal transport and (ii) that the transverse polarization branches are similar and can be described by a unique dispersion relation for a given crystalline direction. The first assumption is regularly done in the modeling of thermal properties of semiconductor materials as optical modes contribution is often weak. In the present cases, for Bi_2Te_3 this was pointed out by Huang and Kaviany [8] who have shown that short-range acoustic phonons (i.e., with a MFP lower than half of their wavelength) and optical ones contribute less than one order of magnitude to TC as compared to long-range acoustic phonons; a similar conclusion was drawn by Chen *et al.* [32] who claimed that heat is mostly carried by acoustic mode with frequency below 1 THz. For the SnSe case, recent studies by Skelton *et al.* [26] and Aseginolaza *et al.* [33] have shown that thermal conductivity is mostly driven by acoustic phonons (around 70% at 300 K) with frequency lower than 3 THz. Consequently, the proposed assumption to simplify modeling is reasonable and will be demonstrated further in the Results and Discussion section. The second hypothesis helps in simplifying the transport model used to solve the BTE with the MC method. For both materials, it will impact the sampled phonon group velocities in the MC procedure, but once again simulation results demonstrate that such assumption weakly affects the computed values and their consistency regarding the experimental data.

A. Bi_2Te_3

The crystal structure of bismuth telluride (Bi_2Te_3) is rhombohedral (space group $R\bar{3}m$) with five atoms per unit cell. It is usually represented as a succession of quintuple layers with a weak bonding of van der Waals (vdW) nature between two Te layers. The hexagonal cell parameters [11] are $a = b = 4.386$ Å and $c = 30.497$ Å. The vdW bonding can be responsible for crystal cleavage and is presently assumed as a supplementary scattering mechanism for phonons in the Γ-Z direction as suggested by Park *et al.* [21]. A detailed description of phonon properties of Bi_2Te_3 can be found in reference studies by Jenkins *et al.* [34] or by Kullmann *et al.* [35].

On the basis of computed or measured acoustic dispersion branches in the Γ-Z and Γ-X directions, one can fit phonon frequencies in the Brillouin zone and make their derivation to evaluate the group velocity. In both directions, it is possible
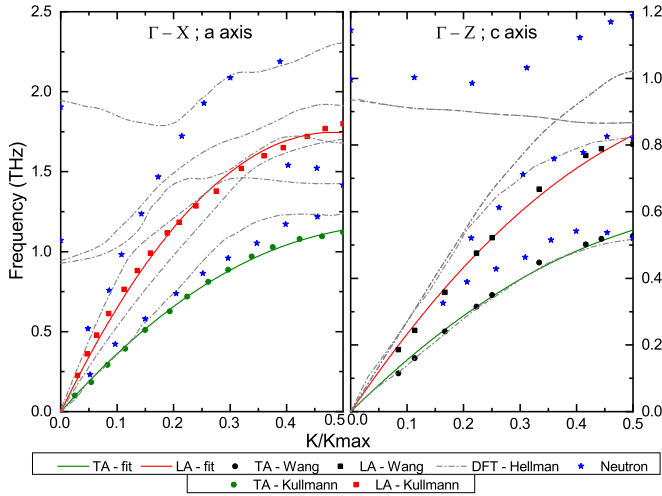
FIG. 1. Bi_2Te_3 acoustic dispersion relations in directions Γ-X and Γ-Z; circles (TA) and squares (LA) are taken from [20,35]; dot-dashed lines are DFT calculations by Hellmann and Broido [9]; stars are INS measurement [35].

to achieve a polynomial regression of phonon frequencies as a function of **K** and obtain the group velocity. First, acoustic dispersion properties in the Γ-Z direction are plotted using data given by Wang *et al.* [20]. A second-order polynomial fit of frequencies is achieved: $\omega_p = v_p K + c_p K^2$ where p is the polarization index, i.e., TA or LA. Similarly, dispersion properties in the Γ-X direction are fitted considering one longitudinal acoustic branch and two identical transverse branches. Along the a axis (basal plane), neutron-scattering experiments and recent DFT calculations [9] show that several branches exist. Here, the latter are averaged on the basis of the work of Kullmann *et al.* [35]. In the latter study, lattice dynamic calculations were conducted and compared with a reasonably good agreement to inelastic neutron-scattering measurements (INS). Those measurements are used as a reference in many studies evaluating phonon dispersion properties in Bi_2Te_3.

Both dispersion curves are presented in Fig. 1. In Table I, the fitting coefficients are reported for each polarization branch.

Phonon group velocities for acoustic branches in the Γ-X and Γ-Z directions are derived from the fitted values. Comparisons to Wang *et al.* [20] are plotted in Fig. 2. The group velocity values obtained by the polynomial fitting of both directions are in the range of reported data in the literature. In Table I, the column v_p gives the velocity at the Γ point; along Γ-Z for the LA branch: 1811, 2283, and 1960 m s^{-1}; and the TA branch: 1774, 1486, and 1370 m s^{-1} were respectively

TABLE I. Quadratic fitting parameters for Γ-X (a axis) and Γ-Z (c axis) dispersion curves of Bi_2Te_3.

Axis	p	v_p (m s^{-1})	c_p (m^2 s^{-1})
Γ-X (a axis)	TA	1324.50	-6.026×10^{-8}
Γ-X (a axis)	LA	2423.25	-1.285×10^{-7}
Γ-Z (c axis)	TA	1756.39	-2.054×10^{-7}
Γ-Z (c axis)	LA	2628.38	-2.297×10^{-7}
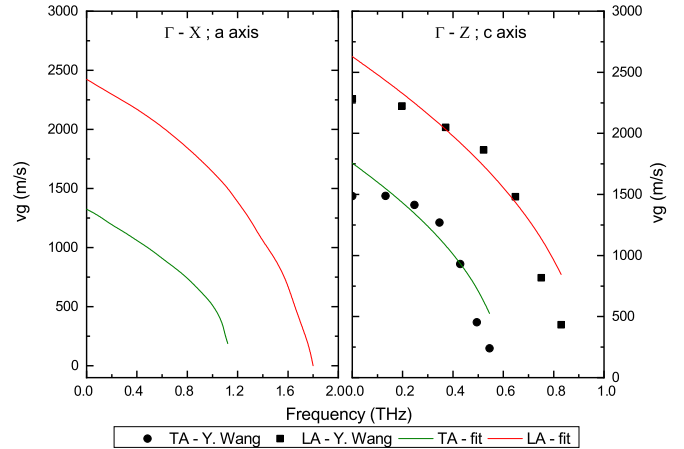
FIG. 2. Bi_2Te_3 group velocities in directions Γ-X (a axis) and Γ-Z (c axis), colored lines; circles and squares are simulated data [20].

reported in [32], [20], and in [9]. Our values somewhat overestimate the DFT-computed values; however, such discrepancy was expected as several studies point out the speed of sound's anisotropy [32,36] in Bi_2Te_3 which cannot be accurately captured with the present model. The sound velocity is deduced from the $1/v_s = 1/3[2/v_{TA} + 1/v_{LA}]$ relation [17]. It reaches 1975 m s^{-1} which corresponds to the ultrasound measurement [36] (1918 m s^{-1}) but remain larger by 10% to the commonly reported values. In the case of the Γ-X direction, there is less available data to achieve comparisons. Hellman and Broido [9] provides 2650 and 1630 m s^{-1} for the LA and TA polarizations, respectively; those values are comparable to those reported in Table I.

B. SnSe

Tin selenide (SnSe) is the second TE material considered in this work. The latter compound is a layered material with an orthorhombic crystal structure [37]. It has two stable phases: the α-SnSe (*Pnma* space group) and the β-SnSe (*Cmcm* space group). The phase transition between α and β-SnSe occurs between 750 and 800 K. In this work, only α-SnSe is considered. It contains eight atoms per unit cell arranged in a zigzag configuration where Sn atoms are surrounded by Se atoms. The lattice parameters of SnSe are $a = 11.49$ Å, $b = 4.44$ Å, and $c = 4.135$ Å, respectively, for the Γ-X, Γ-Y, and Γ-Z directions [38]; the thermal transport properties are studied according to those three main axes; dispersion and lifetime properties are modeled in these specific directions.

SnSe dispersion relations have been fitted using data reported by Zhao *et al.* [23] and computed by DFT within the quasiharmonic approximation. For the three main directions, we assume, as in the previous case, that acoustic branches can be modeled by two identical transverse branches (TA) and a longitudinal one (LA). In practice, the distinction between TA polarizations can be achieved especially for the b and c axes along which phonon velocities change near the Γ point; along the a axis, phonon modes are softened and TA branches remain very similar. Other studies also achieved by DFT [24,26,28] show that dispersion calculation is highly sensitive
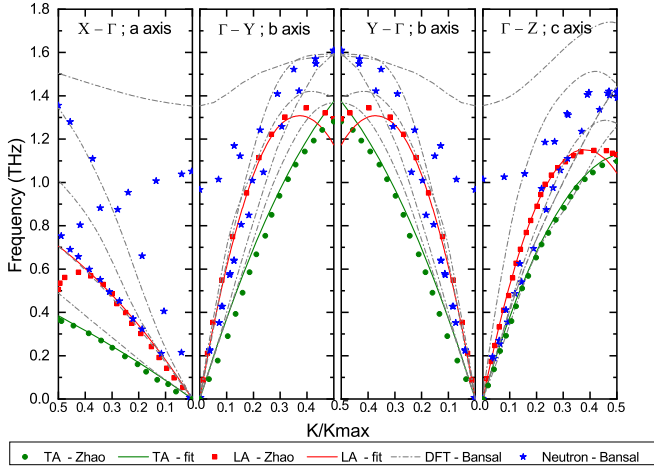
FIG. 3. SnSe acoustic dispersion relations in directions Γ-*X*, Γ-*Y*, and Γ-*Z*; circles and squares are taken from Zhao *et al.* [23] and are used for fitting; DFT calculations by Bansal *et al.* [39]; stars are neutron inelastic-scattering measurements [39].

to the supercell size and the chosen calulation methodology (GGA, LDA, PBE) for electronic exchange correlations. Hence the choice made here, which does not much impact the simulation of thermal transport properties, is supposed to be a reasonable average of phonon behavior in the frame of the kinetic modeling of phonon transport. In addition, inelastic neutron-scattering measurements were carried out by Li *et al.* [39,40]. They partly recover the DFT simulation results along the different axes, in particular phonon mode softening in the Γ-*X* direction when compared to the Γ-*Y* and Γ-*Z* directions. INS also reveals that all phonon modes are obviously softened as the temperature increases while anharmonicity increases [40]. Detailed diagrams of phonon dispersions in SnSe are plotted in Fig. 3, and the quadratic fitting parameters are detailed in Table II.

In order to achieve some comparisons about phonon velocities, we calculate sound velocities in each direction using our fitting parameters (Table II) and the data reported in the supplementary material of the study by Zhao *et al.* [23]. With the quadratic fit the results are as follows: 1233.07 m s^{-1} (*a* axis), 2062.10 m s^{-1} (*b* axis), and 1906.18 m s^{-1} (*c* axis), in comparison, using the DFT-predicted phonon velocities at the Γ point [23], we get 1272.80 m s^{-1} (*a* axis), 1796.55 m s^{-1} (*b* axis), and 1775.38 m s^{-1} (*c* axis). This agreement is satisfactory as the maximum deviation is about 12% for the *b* axis, and remain below 10% otherwise. Variation of

TABLE II. Quadratic fitting parameters for Γ-*X* (*a* axis), Γ-*Y* (*b* axis), and Γ-*Z* (*c* axis) dispersion curves of SnSe.

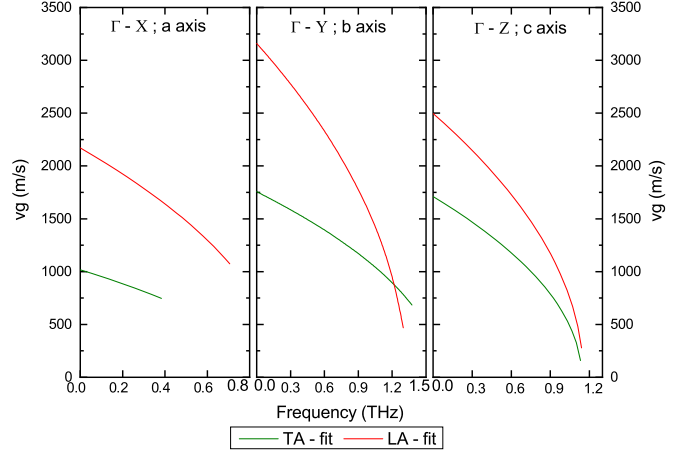| Axis	p	v_p (m s^{-1})	c_p (m^2 s^{-1})
Γ-*X* (*a* axis)	TA	1014.03	-4.950×10^{-8}
Γ-*X* (*a* axis)	LA	2170.98	-2.007×10^{-7}
Γ-*Y* (*b* axis)	TA	1757.04	-7.579×10^{-8}
Γ-*Y* (*b* axis)	LA	3159.09	-2.993×10^{-7}
Γ-*Z* (*c* axis)	TA	1711.04	-1.020×10^{-7}
Γ-*Z* (*c* axis)	LA	2469.43	-2.150×10^{-7}

FIG. 4. SnSe group velocities in directions Γ-*X* (*a* axis), Γ-*Y* (*b* axis), and Γ-*Z* (*c* axis).

the phonon group velocities in each direction are reported in Fig. 4. These values will be used in the MC simulation of phonon transport.

III. SCATTERING LIFETIMES

Analysis of semiconductor thermal conductivity in the frame of simple analytic modeling of phonon scattering is known from the early 1960s with seminal works by Callaway [16] and Holland [17]. This method allows one to overcome complex DFT calculations of lattice vibrations assuming that phonon-scattering processes can be represented by relaxation times depending on frequency and temperature for each scattering mechanism; i.e., normal, umklapp, defect, isotope, etc. However, the technique is constrained by the knowledge of constant parameters associated to each scattering relaxation time. Those parameters can be either evaluated theoretically from the knowledge of crystal structure parameters like the atom average mass M, the Grüneisen parameter γ, the Debye temperature θ_D, and the sound velocity v_s or adjusted to fit the measured TC of bulk samples. In addition, it shall be noticed that the method applies to bulk material even if size effect can be considered through the boundary scattering relaxation time used to compute very low temperature TC. Below some tens of kelvin, the phonon mean free path is so large that other scattering mechanisms are usually weak. This approach was successfully applied to calculate the TC of bulk semiconductors such as Si, Ge, GaN, BN, SiC and others in the frame of the kinetic theory, all relaxation rates being summed according to the Matthiessen's rule. Those relaxation times can be also used to solve the Boltzmann transport equation through the handling of the collision integral term. In the latter approach, several resolution techniques can be used and, more importantly, the material nanostructuration effect can be accounted for. This issue is discussed further in the BTE modeling section.

In the present work, Bi$_2$Te$_3$ and SnSe scattering relaxation times have been implemented following the detailed methodology proposed by Morelli *et al.* [41]. Four distinct scattering processes were considered: the umklapp, the normal, and the impurity/defect ones; moreover, in the case of Bi$_2$Te$_3$

along the c axis, van der Waals scattering was also taken into account as suggested by Park *et al.* [21] to model weak atomic bonding and lower thermal conductivity in this direction.

A. Models for phonon-scattering processes

1. Phonon-phonon umklapp scattering

Umklapp scattering is derived from the formulation proposed by Slack and Galginaitis [42] on the basis of fits comparing theoretical thermal conductivity of several crystals to experimental ones; it reads

$$\tau_U^{-1}(\omega, T) = B_U \omega^2 T \exp\left(\frac{-\theta_D}{3T}\right), \tag{1}$$

where ω is the phonon frequency, T the temperature, θ_D the Debye temperature, and B_U a constant parameter for the umklapp scattering process

$$B_U \simeq \frac{\hbar \gamma^2}{M v_s^2 \theta_D} \tag{2}$$

with $\hbar$ the reduced Planck constant, γ the Grüneisen parameter, M the average mass of an atom in the crystal, and v_s the sound velocity. In this work, the same formulation [Eq. (1)] of the umklapp relaxation rate applies to both TA and LA polarizations. However, in the specific case of TA branches, we consider a limit frequency ω_{lim} below which no umklapp scattering can arise following the Han and Klemens model [43]. This frequency is calculated from the following condition on wave vector $\mathbf{K}_{\mathrm{lim}}/\mathbf{K}_{\mathrm{max}} = 1/2$.

2. Phonon-phonon normal scattering

Phonon normal scattering does not induce resistive processes that inherently affect thermal conductivity and is not always considered in kinetic modeling of thermal transport. However, Callaway's model [16] uses this relaxation lifetime to achieve TC conductivity calculations with kinetic theory. This lifetime is also needed to perform TC calculations with a Monte Carlo method as normal scattering changes phonon population and thus indirectly affects other scattering processes. Several formulations of normal relaxation rates exist; here we consider the model detailed by Asen-Palmer *et al.* [44] that makes a distinction between LA and TA polarizations. For the LA branch, it reads

$$\tau_{N,L}^{-1}(\omega, T) = B_{N,L} \omega^2 T^3, \tag{3}$$

and for the TA one

$$\tau_{N,T}^{-1}(\omega, T) = B_{N,T} \omega T^4. \tag{4}$$

Constant parameters $B_{N,L}$ and $B_{N,T}$ are often adjusted to fit thermal properties. Nevertheless Morelli [41] recalls values that depend on the same crystallographic parameters defined above for B_U and which are used in this study.

$$B_{N,L} \simeq \frac{k_B^3 \gamma^2 V}{M \hbar^2 v_L^5} \tag{5}$$

and

$$B_{N,T} \simeq \frac{k_B^4 \gamma^2 V}{M \hbar^2 v_T^5}, \tag{6}$$

where V is the volume per atom and v_L and v_T are the phonon group velocities for the LA and TA branches, respectively. As will be shown further, the Grüneisen parameter γ is often tuned as the sole adjustment parameter to reproduce experimental TC values. In some studies, γ can be defined with different values for LA and TA modes [41]; we do not make this choice in order to limit the number of adjustable parameters of the phonon scattering model.

3. Phonon-impurity/defect scattering

Impurity (or isotopic) as well as punctual defect scattering are often described using Rayleigh's theory, phonon scattering being proportional to the fourth power of frequency. According to several studies [17,41] for both polarizations, it states

$$\tau_{I/D}^{-1}(\omega) = B_{I/D} \omega^4 \tag{7}$$

with

$$B_{I/D} \simeq \frac{\Gamma V}{4\pi v_s^3} + A, \tag{8}$$

where Γ is the mass-fluctuation phonon-scattering parameter which depends on the isotopic composition of the material and A is a constant parameter for point defect [45]. Details on Γ calculation for both Bi$_2$Te$_3$ and SnSe are provided in the Appendix. These materials are binary compounds and averaging rules shall be considered [41]. The defect-induced scattering magnitude is more complex to evaluate analytically as it is related to the elaboration process used to synthesize materials. In the case of a perfect material such defect scattering shall be null ($A = 0$), but this is no longer true in the more realistic case of compounds with vacancies, antisites, cleavage, etc. The constant A, related to this lifetime, has to be adjusted by comparing experiments and calculations.

4. Phonon–van der Waals scattering

In the specific case of bismuth telluride, along the c axis (Γ-Z) atoms are organized according to repeating quintuple layers (Te$_1$-Bi-Te$_2$-Bi-Te$_1$) for which there are weak van der Waals atoms bounding between each Te$_1$-Te$_1$ layer that separates two successive quintuples. Such bounding limits heat transport along the c axis and partly explains the lower thermal conductivity observed in this direction. In this study, following the Park *et al.* [21] work we add a vdW scattering rate that models resistance to heat transport due to phonon scattering at Te$_1$-Te$_1$ "interfaces." In such approximation, lifetime formulation is similar to what can be used to model superlattices [46], each quintuple being the basic pattern of the multilayered structure

$$\tau_{vdW}^{-1}(\omega) = \frac{4 v(\omega)}{3H} \frac{[1 - t(\omega)]}{t(\omega)}, \tag{9}$$

where v is the group velocity of the LA or TA modes, H is the thickness of one quintuple, and $t(\omega)$ is the phonon spectral transmissivity. The latter quantity needs to be defined by a reliable interface model. For superlattices, acoustic and diffuse mismatch models (AMM and DMM) were often used depending on the interface roughness, the bounding materials, etc. In the present case, transmittivity between Bi$_2$Te$_3$

TABLE III. Input parameters for Bi_2Te_3 relaxation rates along the a and c axes, taken from Refs. [21,34,36].

Parameter	a axis	c axis
θ_D (K)	145 [34]	
γ	1.0–1.17 [36]	1.49 [34]
v_s (m s^{-1})	1559.2	1973.4
ω_{lim} ($\times 10^{12}$ rad s^{-1})	2.1790	4.9030
H (Å)		10.1 [21]
Γ ($\times 10^{-4}$)	60–90	60
V (Å^{-3})	34.0 [21]	
ρ (g cm^{-3})	7.857 [36]–7.8624 [34]	

TABLE IV. Input parameters for SnSe relaxation rates along the a, b, and c axes, taken from Refs. [23,28,38,48].

Parameter	a axis	b axis	c axis
θ_D (K)	215 [28]	180 [28]	189 [28]
γ	1.8	1.8–2.1[23]	1.8
v_s (m s^{-1})	1272.8 [23]	1796.55 [23]	1775.38 [23]
ω_{lim} ($\times 10^{12}$ rad s^{-1})	1.1149	3.5661	4.3790
Γ ($\times 10^{-4}$)	3.882		
V (Å^{-3})	26.472 [38]–26.547 [48]		
ρ (g cm^{-3})	6.050 [38]–6.180 [48]		

quintuples is considered in the frame of AMM modeling with a simplified formulation of Prasher transmissivity given between two distinct materials in contact by weak vdW bonding [47]. In this framework, Park *et al.* [21] have simplified $t(\omega)$ considering the same acoustic impedance $Z = \rho v_s$ on both sides of the quintuple "interface":

$$t(\omega) = 1 \bigg/ \left[1 + \frac{\omega^2}{4K_a}(Z^2 \cos^2 \theta) \right], \qquad (10)$$

where K_a is the spring constant between atoms per unit area and θ the angle between the interface normal and the phonon propagation direction. In Eq. (10) the parameter K_a is defined as $K_a = nK$ with n the number of atoms per unit area and K the stiffness defined as the second derivative interatomic potential $\phi(r)$ for $r = r_0$, the equilibrium bond distance (minimum of the well).

$$K_a = \frac{K}{r_0^2} = \frac{1}{r_0^2} \left. \frac{d^2\phi(r)}{dr^2} \right|_{r=r_0}. \qquad (11)$$

For bismuth telluride, interatomic potential is often a two-body potential that associates a short-range potential and a long-range one for Coulomb interaction [8,10,11]. Short-range potential for Bi_2Te_3 is typically Morse potential, expressed as $\phi(r) = \phi_0[\{1 - e^{[-a(r-r_0)]}\}^2 - 1]$ with ϕ_0 the depth of the potential well and a the bond elasticity. Using this expression of the potential in Eq. (11), the stiffness K and the spring constant per unit area K_a can be calculated as

$$K_a = \frac{2a^2\phi_0}{r_0^2}. \qquad (12)$$

In this work, interatomic potential parameters given by Huang and Kaviany [8] between Te_1-Te_1 layers were used ($\phi_0 = 0.0691$ eV and $a = 2.174$ Å^{-1}, $r_0 = 3.64$ Å), leading to a stiffness $K = 10.465$ N/m and spring constant per unit area of $K_a = 7.8983 \times 10^{19}$ N m^{-3}.

B. Bi_2Te_3 and SnSe relaxation-time parameters

Relaxation rates for all the above discussed scattering processes need constant parameters B_U, $B_{N,L}$, $B_{N,T}$, $B_{I/D}$, and $t(\omega)$, according to Eqs. (2), (5), (6), (8), and (10) for each considered crystalline axis. All these inputs are provided in Table III for Bi_2Te_3 and Table IV for SnSe. In these two tables, data without reference have been taken from our dispersion modeling or adjusted to fit experimental results. This is the

case for the Grüneisen parameter γ which is one of the key fitting parameters of SnSe, as will be shown in the Results and Discussion section.

IV. THERMAL CONDUCTIVITY CALCULATION MODEL

Thermal transport in materials at nano- and microscales as well as thermal properties of nanostructures can be considered by several numerical techniques. The choice of the relevant technique is often dictated by parameters such as size, nature, complexity of the material, etc. The accuracy and reliability of the methods also depend on these considerations. In the frame of atom scale modeling, DFT calculations become more and more popular. They are efficient for bulk material modeling of their intrinsic properties with little input regarding the material itself except its atomic structure and the correlation functional. Drawbacks of DFT are the complexity of use, the very long simulation time, and the fact that it cannot address nanostructuration straightforwardly. A second popular numerical tool for material modeling is MD. This method is now commonly used thanks to extended simulation environments such as LAMMPS [49] or DL-POLY [50] which propose several computation packages. Modeling thermal transport with MD in nanostructures is possible for various objects (film, wire, porous medium, inclusion, etc.) but remains limited to very small sizes as all atoms need to be considered. In addition, physics that depict atom displacements is modeled by interatomic potentials which are rarely available. Within this context, describing thermal transport in nanostructures through the resolution of the Boltzmann transport equation by Monte Carlo simulation is of interest because it allows one to deal with larger size systems within a reasonable computation time. Nevertheless, as with other numerical methods, MC solution of the BTE includes some weaknesses. Among them, the necessity to define relaxation rates to model the collision term of the BTE which includes "calibration stage" on bulk material before proceeding to nanostructure calculations. Details regarding the MC simulation technique implementation can be found in previous works [51–53].

A. BTE for phonons

The Boltzmann transport equation for phonons is related to the variations of the distribution function $f(t, \mathbf{r}, p, \mathbf{K})$ which depends on time t, position $\mathbf{r}$, polarization p, and wave vector $\mathbf{K}$. $f(t, \mathbf{r}, p, \mathbf{K})$ is the mean particle number at time t in the d^3r volume around r with $\mathbf{K}$ wave vector and d^3K accuracy

for a given polarization p. In the absence of external forces, the BTE reads

$$\frac{\partial f}{\partial t} + \nabla_{\mathbf{K}}\omega \cdot \nabla_{\mathbf{r}}f = \left.\frac{\partial f}{\partial t}\right|_{Coll} \tag{13}$$

with the phonon group velocity $v = \nabla_{\mathbf{K}}\omega$ and $f^0(T, p, \mathbf{K}) = 1/[\exp(\hbar\omega/k_BT) - 1]$ the equilibrium thermodynamic phonons population for polarization p and wave vector $\mathbf{K}$, which is described by the Bose-Einstein distribution function. The collision term, in the frame of the relaxation-time approximation, is expressed as

$$\left.\frac{\partial f}{\partial t}\right|_{Coll} = \frac{f^0(T, p, \mathbf{K}) - f(t, \mathbf{r}, p, \mathbf{K})}{\tau(T, p, \mathbf{K})}, \tag{14}$$

where τ is the phonon-scattering relaxation time, which depends on the phonon-scattering mechanisms and dispersion properties. τ is evaluated from Eqs. (1), (3), (4), (7), and (9) according to the relevant scattering mechanism.

B. Monte Carlo modeling

The Monte Carlo procedure requires successive stages which are reproduced for each time step of the simulation until the convergence (steady-state temperature and heat flux) is reached. The nanostructure geometry is defined and meshed with rectangular cells of volume V_{cell}; the nature of the structure (film or wire) is defined through the chosen boundary conditions that can be either specular or diffuse [51,52]. When all BCs are specular, we access cross-plane TC; when two BC's are specular and the other ones diffuse we access in-plane TC; and eventually when all BC's are diffuse, we can compute nanowire TC. Once the geometry is set, the temperature gradient at the edges of the nanostructure (first and last cells) is set and the energy within each cell is calculated from the Bose-Einstein distribution and the density of states. When the initialization of the system is achieved, phonon packets (bundles) are randomly drawn from a cumulative distribution function that depends on the material dispersion properties. Each bundle has a distinct frequency, polarization, group velocity, and initial propagation direction. At each simulation time step, bundles are allowed to drift and scatter according to a collision probability $P_{Coll} = [1 - \exp(-\delta t/\tau)]$ where δt is the simulation time step. When a steady state is reached, phonon heat flux within the structure is calculated with $\varphi_z = \Sigma_{i=1}^{\mathcal{N}}(\hbar\omega_i v_{z,i})/V_{cell\ i}$ where $\mathcal{N}$ is the number of phonon bundles in each cell. Thermal conductivity k is derived from Fourier's formalism knowing the heat flux φ_z and the temperature gradient. Typically, nanostructures made of 20 cells that contain $\simeq 10^4$ bundles per cell ensure statistical accuracy. The number of time steps depends on the material and the length of the nanostructure. An important issue is the choice of simulation time step δt; the latter has to be as small as possible to avoid "excessive" scattering occurrences which lead to an artificial increase of the computed TC. The choice of time step is closely related to the phonon lifetime; in practice P_{Coll} shall be lower than 10%.

In the next section, the results of TCs computed by this MC approach for both Bi$_2$Te$_3$ and SnSe nanostructures are provided.

TABLE V. Relaxation rate constants for Bi$_2$Te$_3$ along the a and c axes, derived from Sec. III.

Constant	a axis	c axis
B_U ($\times 10^{-18}$ s K^{-1})	1.1249	1.5801
$B_{N,L}$ ($\times 10^{-22}$ s K^{-3})	3.6038	5.3982
$B_{N,T}$ ($\times 10^{-10}$ K^{-4})	9.6811	5.3119
$B_{I/D}$ ($\times 10^{-42}$ s^3)	4.2575–6.3862	2.0999
Z ($\times 10^6$ kg m^{-2} s^{-1})		9.0119–9.9283

V. RESULTS AND DISCUSSION

Several kinds of nanostructures were considered in this study. Before dealing with size effects that allow reduction of the TE material TC we have to assess the reliability of the proposed model to recover thermal transport properties in bulklike materials. To meet this purpose, TE films with a thickness of 1μm are considered.

A. Thick film cross-plane thermal conductivity versus temperature

1. Bi$_2$Te$_3$

We compute the cross-plane thermal conductivity of Bi$_2$Te$_3$ along the a and c axes for temperatures in the range of 100–500 K. MC simulations were compared to the existing literature data on both experimental [54–56] and simulation [8,10] sides.

In Fig. 5 are plotted calculated TC values for the a axis [Fig. 5(a)] and the c axis [Fig. 5(b)] as a function of temperature. In both cases, agreement with the experimental data detailed in former studies [54–56] is satisfactory.

Regarding the case of thermal transport in the basal plane (Γ-X), the computed k values were obtained with the lifetimes reported in Table V.

Constants B_U, $B_{N,L}$, and $B_{N,T}$ were calculated using Eqs. (2), (5), and (6), respectively, without any adjustment. The constant $B_{I/D}$ related to impurity/defect scattering was tuned changing Γ the mass-fluctuation phonon-scattering parameter in a ratio of 1 to 1.5 in order to fit experimental data reported by Goldsmid [54] and Satterthwaite [55]. The latter parameter can be evaluated theoretically considering isotopic composition of Bi and Te atoms using Klemens and Slack models for a binary compound. The computed theoretical Γ_{th} value is equal to 0.83×10^{-4} as isotopic disorder is mostly related to Te. The latter Γ value is small and cannot capture low-temperature scattering mechanisms solely. However, as mentioned recently by Liu $et\ al.$ [57], in addition to isotopic impurity scattering other classical zero-dimensional defects such as interstitial, vacancies, and antisites shall be considered. Furthermore, the van der Waals nature of layered growth in Bi$_2$Te$_3$ can easily give rise to dislocation (one-dimensional defects). In this regard, comparison of modeled thermal conductivity to experimental values can be reconsidered by increasing the impurity/defect scattering rate. In Fig. 5(a), MC calculations labeled "case 1" and "case 2" stand for Γ values of 6×10^{-3} and 9×10^{-3}, respectively. The shaded area gives the range of variation of thermal conductivity computed by MC for Γ varying between those two values. Increasing Γ
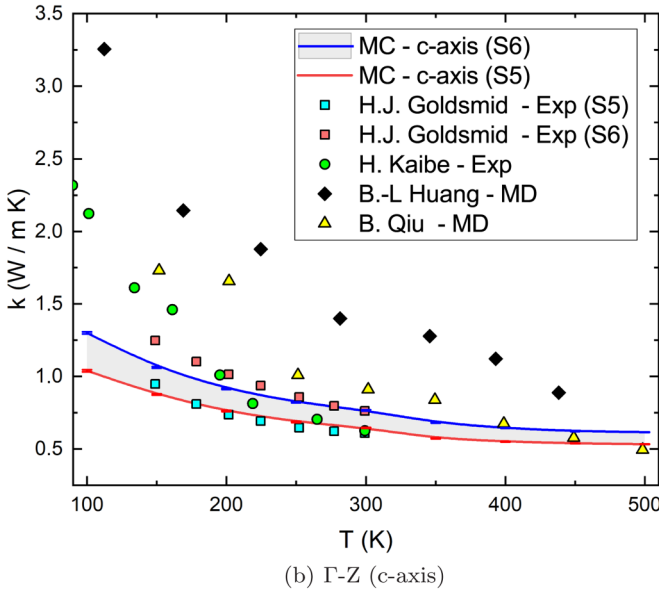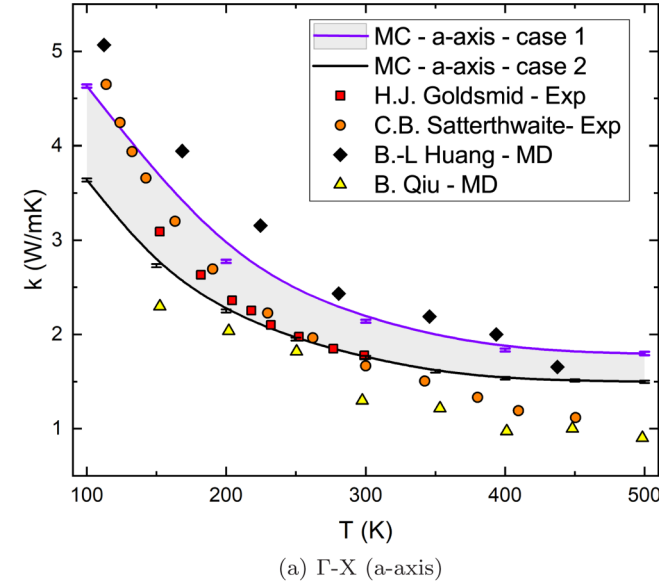
(a) Γ-X (a-axis)

(b) Γ-Z (c-axis)

FIG. 5. Bi_2Te_3 thermal conductivity along Γ-*X* (*a* axis) and Γ-*Z* (*c* axis). Experimental data (samples S5 and S6) by Goldsmid [54], Satterthwaite and Ure [55], and Kaibe *et al.* [56]; MD data by Huang and Kaviany [8] and Qiu and Ruan [10].

will further decrease *k* on the whole temperature range with a weaker effect at high temperatures where umklapp scattering dominates.

In Fig. 5(b), thermal conductivity perpendicular to the basal plane (*c* axis) is plotted in the same temperature range. In the Γ-*Z* direction, TC is lower than along the Γ-*X* direction; this result is confirmed here. Constant parameters for lifetime calculation are reported in the second column of Table V with no adjustment. In addition to classical relaxation rates, in this direction, we also consider van der Waals scattering between quintuples. The latter mechanism depends on phonon transmissivity $t(\omega)$, Eq. (10), which includes angular dependence through the angle θ between phonon propagation direction and the interface normal. The latter dependence is not straight-
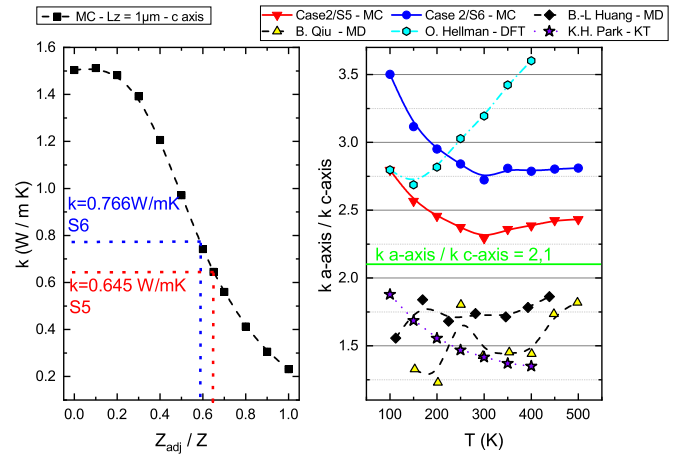

FIG. 6. Left: Thermal conductivity along the *c* axis at 300 K for adjustment of acoustic impedance in Eq. (10). Right: Thermal conductivity anisotropy between the Γ-*X* and Γ-*Z* directions; comparison of MC, MD [8,10], KT [21], and DFT [9] modeling.

forward to implement in MC calculation as we do not consider local atomic description of the quintuples as in MD. We thus adjust the $\cos^2 \theta$ value to recover the experimental data given by Goldsmid [54] and Kaibe *et al.* [56], defining an adjusted acoustic impedance $Z_{adj} = Z \cos^2 \theta$. In Fig. 6 (left) are plotted the thermal conductivity at 300 K for the Z_{adj}/Z ratio varying from 0 to 1. *k* values of 0.645 and 0.766 W m^{-1} K^{-1} correspond to the Goldsmid [54] measurements for the S5 and S6 samples at room temperature; the corresponding Z_{adj}/Z ratios are 0.65 and 0.59, respectively. Averaging $\cos^2 \theta$ between 0 and $\pi/2$ gives $Z_{adj}/Z = 0.5$, which is close to the adjusted values. Using this fitted parameter, the thermal conductivity is then computed for both cases (S5 and S6) at different temperatures showing good agreement above 200 K. At lower temperatures our modeling starts to underestimate the experimental TC values. Nevertheless, MC simulation results provide a better estimation of TC than available MD taking into account its classical nature.

Lastly, the thermal conductivity anisotropy between the Γ-*X* and Γ-*Z* directions is plotted in Fig. 6 (right) calculating the $k_{a\text{-axis}}/k_{c\text{-axis}}$ ratio with MC simulation results for the above-mentioned labels case 2, S5, and S6. The TC anisotropy in bulk Bi_2Te_3 was measured by Goldsmid [58] around $k_{a\text{-axis}}/k_{c\text{-axis}} = 2.1$. Our MC simulation results (case 2, S5) are in relatively good agreement with this value in the range of 200–500 K, while MD simulations [8,10] and kinetic theory [21] underpredict this value. Oppositely, DFT calculations [9] overestimate the anisotropy ratio of thermal conductivity.

2. SnSe

Monte Carlo simulations of tin selenide thermal transport at nanoscales were conducted in a very similar way to those achieved on bismuth telluride. All lifetime constants for the three main axes have been computed with a reduced, as possible, number of adjustment parameters. Before going into detail on the simulation results, it can be recalled that the experimental measurement achieved on SnSe was controversial
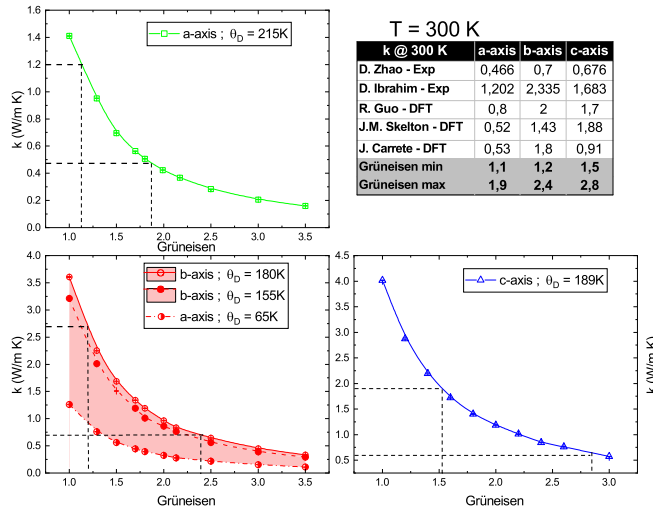
FIG. 7. Monte Carlo simulations of SnSe thermal conductivity at 300 K as a function of the Grüneisen parameter. Inset table: Thermal conductivities at 300 K in SnSe from experiments [23,29] and DFT calculations [24–26].

as sample preparation can substantially change the measured thermal conductivities. In the following, we will show that the dispersion of measured thermal conductivity can be related to the variation of a single parameter, the Grüneisen constant.

SnSe used as a thermoelectric material has received a renewed interest for several years as recent work by Zhao *et al.* [23] shows that the figure of merit value of $ZT = 2.62$ could be achieved along the b axis at high temperatures ($\simeq 900$ K). Among other parameters, low lattice thermal conductivity of SnSe was pointed out as a major reason for the high conversion efficiency. In connection with this work, several other studies were carried out experimentally [29,30,59] and numerically [24–26,28] to try to understand the underlying mechanisms that reduce TC, but also to reproduce the latter observations. A main result of these subsequent works is the broad range of measured and computed TCs. In Fig. 7, the inset table reports k values obtained at 300 K in different studies. Discrepancies between the observations were possibly attributed to material density [31], microstructure, surface oxidation, and defect/vacancies occurrence. However, no definitive reason was pointed out as an explanation for the variety of measured TC in SnSe. In this context, the purpose of our work is not to propose an additional model that confirms or overturns previous studies but to provide indications about the material intrinsic parameters used in simulation that can explain such dispersion of TC.

Umklapp and normal scattering processes are explicitly varying with Grüneisen parameter γ; its choice is crucial to carry out thermal conductivity calculations. In addition, Debye temperature θ_D also affects the evaluation of the umklapp relaxation rate [Eqs. (1) and (2)]. In the literature about SnSe, both γ and θ_D parameters were defined with very different values (see Table VI) according to the considered evaluation procedure.

In the present work, we choose to set the value of the Debye temperature for which there is a better general agreement with experimental measurements (averaged $\theta_D = 210$ K) accord-

TABLE VI. Grüneisen parameter γ and Debye temperature θ_D for SnSe along the a, b, and c axes reported in the literature.

Reference	γ			θ_D (K)		
	Γ-X	Γ-Y	Γ-Z	Γ-X	Γ-Y	Γ-Z
Guo *et al.* [25]	2.12	1.55	1.66			
Zhao *et al.* [23]	4.1	2.1	2.3	24	65	58
Liu *et al.* [60]	1.26	1.29	0.46			
Bansal *et al.* [39]	1.44	1.35	0.64			
Xiao *et al.* [61]		2.83			142	
González-Romero *et al.* [28]				215	180	189

ing to González-Romero *et al.* [28]. The impact of θ_D variation on the SnSe TC at 300 K can be observed in Fig. 7 along the b axis for which three cases were considered ($\theta_D = 65$ K, $\theta_D = 155$ K, and $\theta_D = 180$ K). For θ_D ranging between 155 and 180 K, k varies by $\simeq 10\%$ whatever is the choice of γ.

For our modeling, the only free parameter thus became the Grüneisen one. In Fig. 7, we plot for the three axes the TC versus γ at 300 K. In the inset table is given the range of γ variation (gray rows) to recover thermal conductivity obtained through experiments and DFT simulations. An average value of $\gamma = 1.8$ gives reasonable agreement with the previously published data on SnSe TC at room temperature. However, other methods derived from elasticity theory or from DFT calculation averaging also allow one to evaluate γ (see Appendix A 1); they provide consistent results with our findings. In this frame, parameters used for lifetime calculation are reported in Table VII using Table IV inputs.

In the following, the thermal conductivity of SnSe thick film is discussed. We will show that the existing dispersion of k values can be partly understood through the variation of the Grüneisen parameter. In Fig. 8 are plotted the calculated TCs along the three above considered axes with a comparison of our MC results to experimental data [23,29] and DFT simulations [24,26]. First, it can be noticed that the thermal conductivity anisotropy pointed out in former studies is also observed with MC simulation. Thermal conductivity along the a axis [Fig. 8(a)] is clearly below that along the b and c axes.

In each subfigure, the gray shaded area corresponds to MC simulations with varying Grüneisen parameter γ and the blue dotted lines relate to MC calculation with $\gamma = 1.8$. In Fig. 8(a), it can be seen that a light variation of $1.7 \leqslant \gamma \leqslant 1.9$ allows one to recover TC values predicted by DFT [24,26] and Zhao measurements [23]. Along this direction, comparison to Ibrahim *et al.* [29] data is more delicate as only low-temperature regime was measured. However, an

TABLE VII. Relaxation rate constants for SnSe along the a, b, and c axes, derived from Sec. III. Constants were computed for $\gamma = 1.8$.

Constant	a axis	b axis	c axis
B_U ($\times 10^{-18}$ s K^{-1})	5.9774	3.5836	3.4948
$B_{N,L}$ ($\times 10^{-21}$ s K^{-3})	2.7265	0.4181	1.4330
$B_{N,T}$ ($\times 10^{-8}$ K^{-4})	1.5817	0.1174	0.1174
$B_{I/D}$ ($\times 10^{-43}$ s^3)	4.2151	1.4984	1.5532
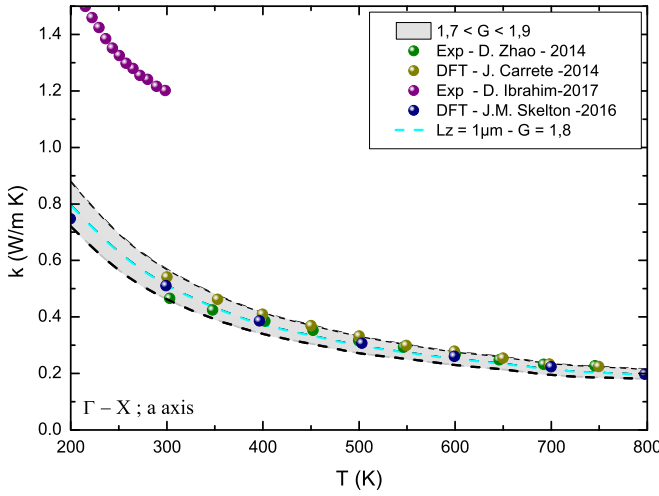
(a) Γ-X (a-axis)
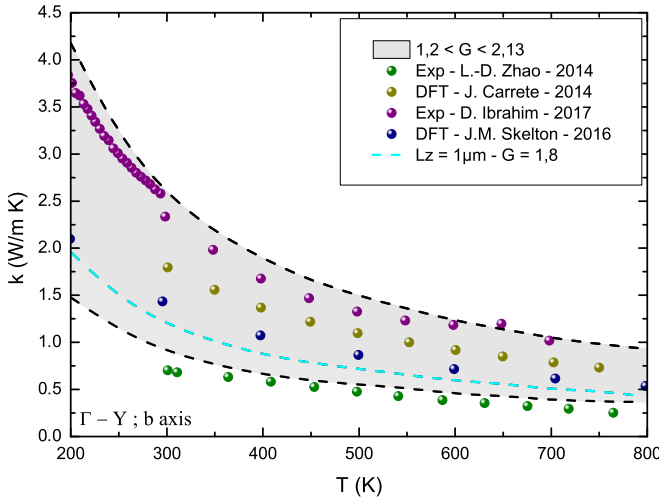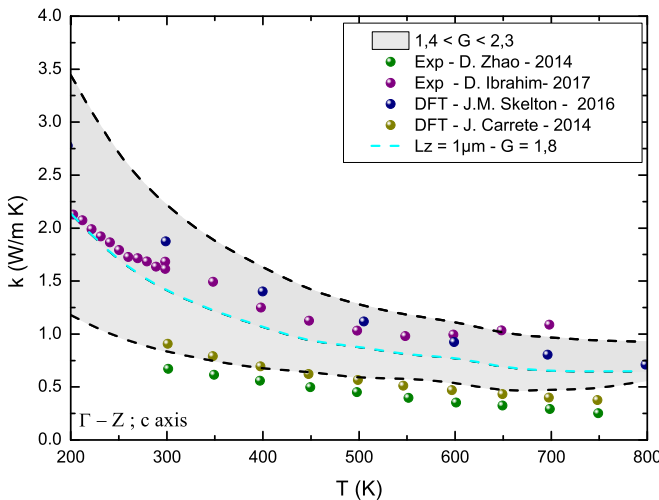
(b) Γ-Y (b-axis)

(c) Γ-Z (c-axis)

FIG. 8. SnSe thermal conductivity along Γ-*X* (*a* axis), Γ-*Y* (*b* axis), and Γ-*Z* (*c* axis). Experimental data [23,29]; DFT data [24,26].
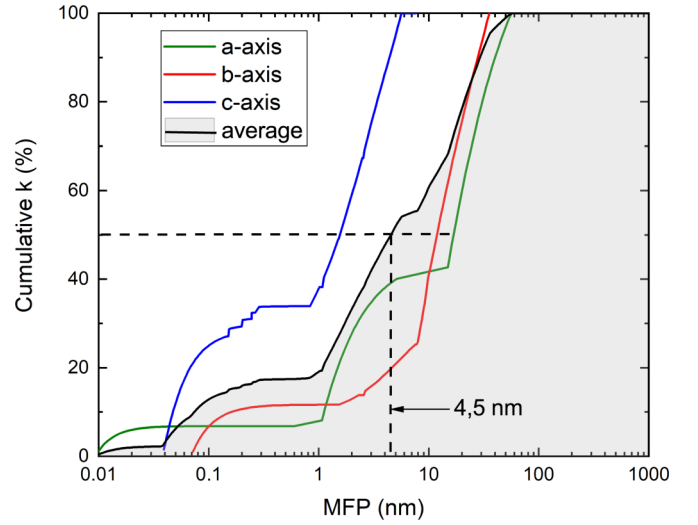
FIG. 9. SnSe cumulative thermal conductivity along Γ-*X* (*a* axis), Γ-*Y* (*b* axis), and Γ-*Z* (*c* axis) for $T = 300$ K as a function of the phonon mean free path. Shaded area: Isotropically averaged value of accumulated thermal conductivity.

expected lowering of γ until 1.1 seems to be necessary to approach the latter TCs. In the case of the Γ-*Y* direction, the experimentally and numerically obtained thermal conductivities roughly differ by a factor of 3 [see Fig. 8(b)]. Such variations can be captured by tuning the Grüneisen parameter in the range $1.2 \leqslant \gamma \leqslant 2.1$ with the lower TC obtained for the larger γ value. This behavior is coherent with the reported literature results and the possible mismatch attributed to non-fully dense SnSe samples. In our calculation, as well as in the study by Zhao *et al.* [23], $\gamma = 2.1$ along the *b* axis is necessary to recover the very low thermal conductivity. Considering the thermodynamic definition of the Grüneisen parameter [Eq. (A1)], γ is inversely related to density ρ; for temperatures larger than 300 K we can assume that the volume thermal expansion coefficient, bulk modulus, and specific heat capacity ratio $\alpha K / C_p$ are almost constant. Thus, as a rough approximation, larger γ is consistent with lower ρ. Oppositely, if we consider smaller γ values in the Γ-*Y* direction ($1.29 \leqslant \gamma \leqslant 1.55$) as suggested by several groups (see Table VI), thermal conductivity notably increases in the whole temperature range. Similar comments apply to the calculated TC in the Γ-*Z* direction [see Fig. 8(c)]. For the latter case, thermal conductivity varies within the same range as in the Γ-*Y* direction. With the MC simulation approach we take a Grüneisen parameter in the range $1.4 \leqslant \gamma \leqslant 2.3$, which allows one to recover most of the literature results. A deeper investigation regarding acoustic phonon transport in SnSe can be achieved by computing the cumulative thermal conductivity as a function of the phonon mean free path (see Fig. 9). The accumulated TC is derived from MC simulation results at 300 K. In order to achieve such calculations we have split the acoustic frequency domain into 100 uniform bins, and recorded the phonon heat flux in each bin during all the simulation processes. Cumulative TC thus results from spectral heat flux contribution with respect to the applied temperature gradient. In order to achieve a comparison between
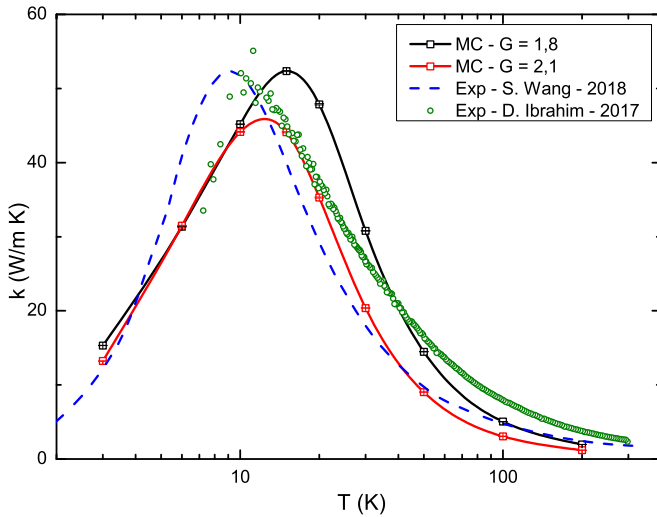
FIG. 10. SnSe thermal conductivity along Γ-Y (*b* axis) at low temperatures. Comparison to experimental data [29,30].

FIG. 11. Bi$_2$Te$_3$ cross-plane thermal conductivity along Γ-X (black lines) and Γ-Z (red line for the S5 case and blue line for the S6 case) at $T = 300$ K; solid lines stand for TC and dotted lines for dimensionless TC.

the three main axes, cumulative TC is normalized. The phonon MFP is directly given by the phonon lifetime and group velocity knowledge assuming Matthiessen's rule. In addition, in order to achieve a comparison with the literature we also plot isotropically averaged cumulative thermal conductivity (shaded gray region) for both plots. It can be noticed that only phonons with $0.1 \leqslant$ MFP $\leqslant 100$ nm contribute to the thermal transport, but their distribution changes according to the crystalline direction. Along the *a* axis, as observed by Carrete *et al.* [24] and Guo *et al.* [25], the contribution of a longer MFP to the total TC is noticeable. In addition, similarly to these two previous studies, cumulative TC with the smallest MFP is observed along the *c* axis. Making isotropic average of cumulative TC (shaded area) also prove the reliability of MC modeling as median *k* accumulation is achieved for MFP ~ 4.5 nm at 300 K, while Guo *et al.* [25] found 4.9 nm and Skelton *et al.* [26] found 3 nm. Such variations of thermal conductivity as a function of energy carriers MFP will be considered in the following sections devoted to the nanostructuration of SnSe samples. In addition, it also validates our modeling choices regarding the thickness of the thin film simulated by the MC method (presently $L_z = 1\,\mu$m), which is much larger than the longest observed phonon MFP.

Eventually, we test our modeling approach to available experimental data about low-temperature thermal conductivity in SnSe. The latter investigations are not numerous. Two recent studies were focused on this issue in the particular case of the Γ-Y axis [29,30]. In Fig. 10 are plotted the TC experimentally obtained by Ibrahim *et al.* [29] and Wang *et al.* [30]. For both experimentations, thick SnSe samples were characterized with a similar device (PPMS, Quantum Design) for temperatures in the range 2–300 K. On the experimental side, it can be noticed that small differences exist between the two studies, even if the maximal TC, ~ 50 W m^{-1} K^{-1} is reached for a temperature close to 10 K. This shift might be due to sample preparation or thermal conductivity recording during the experiments. However, the purpose of our modeling is not to confirm or dispute the
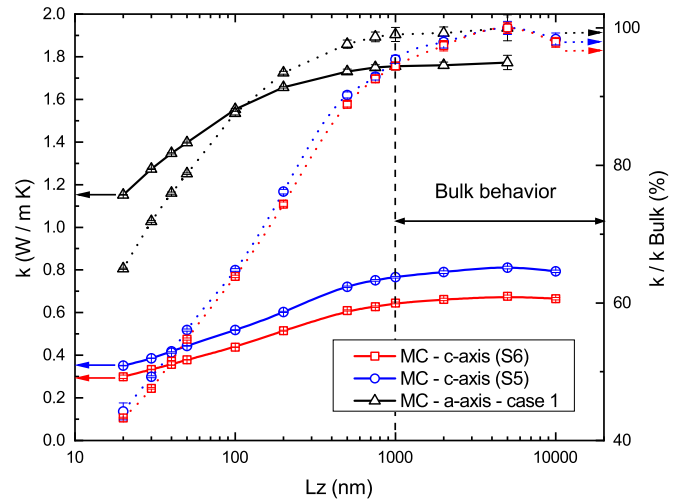
experimentally evaluated TCs but rather to observe the ability of MC modeling to reproduce low temperatures evolution of *k*. Comparisons with the MC modeling were done assuming two distinct Grüneisen parameters: $\gamma = 1.8$ and $\gamma = 2.1$. It can be observed that the thermal conductivity computed for larger γ underpredicts experimental values from 10 to 300 K; better achievement is obtained with $\gamma = 1.8$. To improve our calculations isotope/defect scattering lifetime could be tuned to fit the experimental TC in the low-temperature regime where such mechanisms predominate.

B. Film cross-plane thermal conductivity versus thickness

On the basis of previously discussed models, the cross-plane thermal conductivity of thin films with various thickness was computed for both compounds. In Figs. 11 and 12, Bi$_2$Te$_3$ and SnSe TCs are respectively given for thicknesses
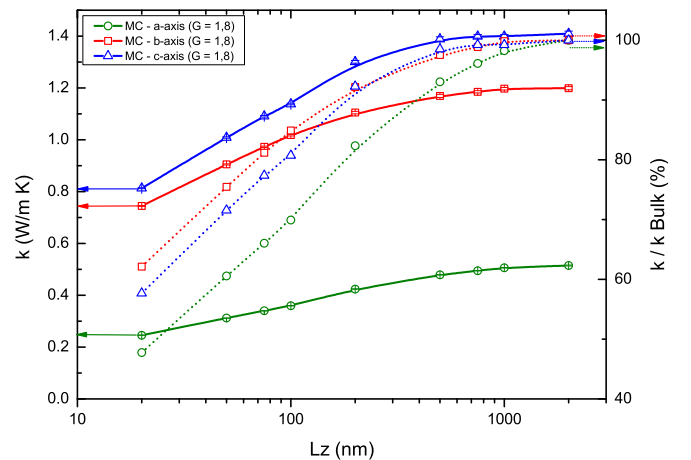

FIG. 12. SnSe cross-plane thermal conductivity along Γ-X (*a* axis), Γ-Y (*b* axis), and Γ-Z (*c* axis) at $T = 300$ K; solid lines stand for TC and dotted lines for dimensionless TC.

in the range of $20 \leqslant L_z \leqslant 10\,000$ nm. In addition, each figure displays the thermal conductivity reduction with phonon confinement given through the ratio k/k_{Bulk} (dotted lines).

For both materials, as expected, for thicknesses above $1\,\mu$m thermal conductivities are constant and supposed to be equal to the bulk ones. This is consistent with previous studies showing that average phonon mean free path is usually well below 100 nm in these thermoelectric materials. For Bi_2Te_3, thermal conductivity lowering is more efficient along the c axis and can reach up to 60% for very thin films of thickness $L_z = 20$ nm. Along the a axis, the maximum achieved TC reduction is about 40% for the thinner simulated films. For such lengths transport is mainly ballistic and is ruled by the thickness of the modeled sample. For very long samples (5 and $10\,\mu$m in Bi_2Te_3) it takes long to reach steady state. Typically, more than 500 000 iterations of 1 ps were needed to start to stabilize heat flux within the structure; this explains the biggest uncertainties recorded for these points. Literature results about TC in thin Bi_2Te_3 films are not numerous. Here we can compare our results to those of nanocrystalline bismuth telluride–based thin films elaborated by flash evaporation [62] or pulsed laser deposition [63]. In the latter works fine crystalline Bi_2Te_3 grains with diameters in the range of 10–60 nm were used to produce the micron-size films. In their studies they found k values along the c axis of 0.2, 0.28, 0.34, and 0.4 W m^{-1} K^{-1} for grain diameters of 10, 27, 33, and 60 nm, respectively. The latter results match our findings.

For SnSe literature concerning nanostructures thermal properties measurement is much less abundant, especially in what concerns nanofilms. In the next section we will show that some measurements were recently done on nanowires [64]. However, in the frame of the current modeling it is interesting to address this issue and try to be predictive in what concerns thermal conductivity reduction when SnSe film thickness is decreased. In Fig. 12 are plotted TCs and dimensionless TCs for the considered axis in films with thicknesses in the range of $20 \leqslant L_z \leqslant 2000$ nm for $T = 300$ K. Here and in the following we consider constant Grüneisen parameters: $\gamma = 1.8$. As expected, the decrease of L_z comes with a decrease of k for the same reasons as discussed above in Bi_2Te_3. Yet, these tendencies are not the same in the three directions. The k/k_{Bulk} ratio clearly shows that TC decrease is much more important for the Γ-X direction for which phonons with large mean free paths exist (up to more than 100 nm; see Fig. 9) that contribute significantly to the TC. Thus in this direction up to 50% of TC lowering is reached. In the other directions, variations are in the same range and ultrathin layers ($L_z = 20$ nm) have k values close to 0.5 W m^{-1} K^{-1}.

C. Nanowire thermal conductivity versus side length

Finally, nanowires are considered. Such nanostructures appear to be more efficient for thermoelectric purposes as they induce more phonon confinement than nanofilms and thus larger TC reduction. In addition, nanowire elaboration can be easier to achieve using processes that rely on electrochemical growth in porous matrices (alumina or polymer) [22] or direct catalyst-assisted growth [64]. In Fig. 13 are plotted the bismuth telluride nanowires thermal conductivity
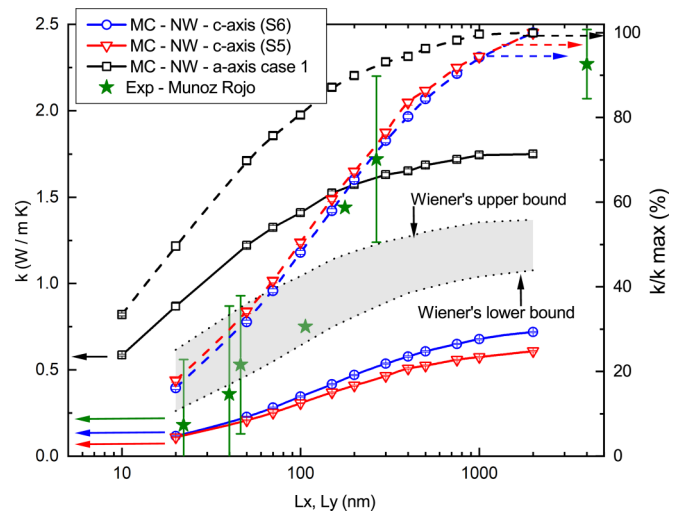

FIG. 13. Bi_2Te_3 nanowire thermal conductivity along Γ-X (black lines) and Γ-Z (red line for the S5 case and blue lines for the S6 case) at $T = 300$ K. Comparison to experimental data by Munoz Rojo *et al.* [22]. The gray shaded area corresponds to the lower and upper bounds of the Wiener's model of effective thermal conductivity.

along the a and c axes; in addition, experimental data reported by Munoz Rojo *et al.* [22] are also added. The latter values correspond to nanowires with a crystalline orientation measured as [110] (perpendicular to the c axis). For our MC simulation, nanowires with square sections ($L_x \times L_y$) are considered. We set diffuse phonon scattering at the lateral nanostructure boundaries [52]; their length is $L_z = 1\,\mu$m for both materials. Once again strong TC reduction can be achieved, i.e., up to 80% for the thinnest wire (square section of 20×20 nm). This trend is also experimentally recovered with even lower k for wire with a diameter of $d \simeq 25$ nm ($k = 0.18 \pm 0.38$ W m^{-1} K^{-1}). However, measurement uncertainty for such small sizes is quite large and modeling gives quite reasonable agreement of the TC. In addition, in order to take into account possible polycrystalline orientation of the material we have plotted the limiting bounds of the sample TC in the frame of Wiener's model. The lower bound (or harmonic mean) is given as $\frac{1}{k_{HM}} = \frac{1}{3}(\frac{1}{k_X} + \frac{1}{k_Y} + \frac{1}{k_Z})$, and the upper bound (arithmetic mean) is $k_{AM} = \frac{1}{3}(k_X + k_Y + k_Z)$. In the case of Bi_2Te_3, the a-axis contribution is counted twice. For such polycrystalline nanowires, literature results [22] are between 1.1 and 1.47 W m^{-1} K^{-1} for nanowires with diameters of 250 and 360 nm, respectively. This is consistent with the bounding limits of the Wiener's model.

In Fig. 14 the TC values for SnSe nanowires are reported. As in the case of cross-plane TC calculation, a strongest lowering of k is observed along the a axis. Here it reaches 80% for the thinnest wire. Along the b and c axes, the evolution of k is similar. When compared to the recent experimental results provided by Hernandez *et al.* [64] for nanowires oriented along the [111] direction we can notice a good agreement of the effective thermal conductivity computed with the Wiener's lower and upper bounds in a large diameter range. In the latter comparison, effective thermal conductivities are obtained combining MC results along the a, b, and c axes.
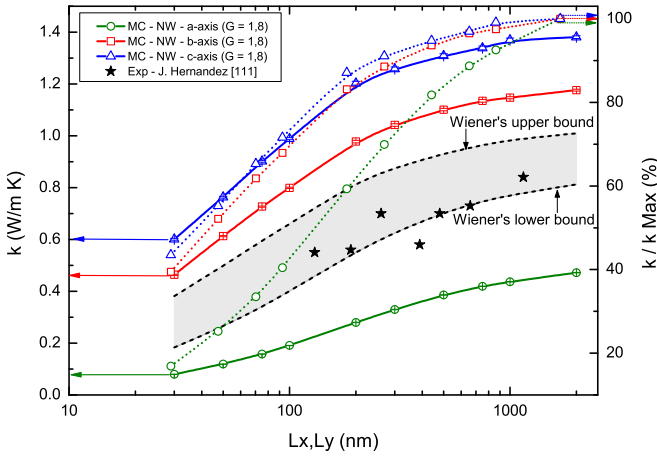
FIG. 14. SnSe nanowire thermal conductivity along Γ-X (*a* axis), Γ-Y (*b* axis), and Γ-Z (*c* axis) at $T = 300$ K. Comparison to experimental data by Hernandez *et al.* [64] in the [111] direction. The gray shaded area corresponds to the lower and upper bounds of the Wiener's model of effective thermal conductivity.

Further comparisons with experimental measurements will be interesting to confirm the model's ability to predict TC in such nanostructures.

VI. CONCLUSIONS

Through this study we propose a modeling approach for thermal conductivity calculation of thermoelectric nanostructures based on the phonon lifetimes formalism and the resolution of the Boltzmann transport equation by Monte Carlo simulations. This methodology lies on the knowledge of material intrinsic parameters, i.e., dispersion properties and atomistic structural parameters, following the general frame of the Debye-Callaway theory. The proposed models were successfully used for bismuth telluride and tin selenide TE compounds, fitting phonon dispersions along main crystalline axes. As adjustment terms, only the Grüneisen parameter γ for SnSe and the mass fluctuation scattering parameter Γ for Bi$_2$Te$_3$ allow one to recover the thermal conductivity of bulk compounds in an extended temperature range with good concordance. Furthermore, we point out that the choice of Grüneisen parameter γ can be seen as a tuning quantity that impacts phonon anharmonicity and thus thermal conductivity in connection with material density. In a second part of this work, the ability of the Monte Carlo method to solve the Boltzmann transport equation for phonons allows us to tackle the problem of heat transport in thermoelectric nanofilms and nanowires. For the latter, an obvious reduction of thermal conductivity due to phonon confinement is observed, and cumulative thermal conductivity in SnSe is directly evaluated from the MC resolution process. Moreover for both materials, the modeling allows one to recover experimental measurements achieved on crystalline nanowires. Improvement of the method will be to deal with three distinct polarization branches for each considered crystalline axis and to take into account grain boundary scattering to model polycrystalline samples. Further development of the method will address

other materials nanostructuration; among them nanoporous thermoelectric materials are of paramount interest.

APPENDIX

1. Grüneisen parameter calculation

The Grüneisen parameter is related to the vibrational frequencies of atoms that change with varying the volume of a solid; it can be evaluated by different methods. A thermodynamic definition of γ is

$$\gamma = V \left. \frac{\partial P}{\partial E} \right|_V = \frac{1}{\rho} \frac{\alpha K}{C_p}, \tag{A1}$$

where V is the volume, P the pressure, E the energy, α the volume thermal expansion coefficient, K the bulk modulus, and C_p the heat capacity at constant pressure. In the framework of the elasticity theory, the Grüneisen parameter [65] for bulk crystalline solids can be derived from the Poisson ratio ν which depends on longitudinal and transverse acoustic velocities according to

$$\gamma = \frac{3}{2} \left(\frac{1 + \nu}{2 - 3\nu} \right) \tag{A2}$$

and

$$\left(\frac{v_{LA}}{v_{TA}} \right)^2 = \left(\frac{2 - 2\nu}{1 - 2\nu} \right). \tag{A3}$$

According to recent literature about the mechanical properties of bulk SnSe [66], its Poisson ratio ν is about 0.22–0.23, meaning that the average Grüneisen parameter according to Eq. (A2) is about $\gamma = 1.4$. Eventually, it is also possible to assess γ directly from DFT calculations. It can be averaged on all the phonon modes with respect to volumetric specific heat. This was achieved by Guo *et al.* [25]; corresponding γ values are given in Table VI in the range 1.55–2.12.

2. Mass fluctuation phonon-scattering parameter calculation

The mass fluctuation phonon-scattering parameter Γ contributes to the point defect scattering and can be calculated using the following equation:

$$\Gamma = \Sigma_i c_i \left[\frac{m_i - \overline{m}}{\overline{m}} \right]^2 \tag{A4}$$

with $\overline{m} = \Sigma_i c_i m_i$ and where m_i is the atomic mass of the *i*th isotope, and c_i is the fractional atomic natural abundance. SnSe material is composed of two atoms; in this case the above equation can be written as

$$\Gamma(\text{SnSe}) = 2\left[\left(\frac{M_{\text{Sn}}}{M_{\text{Sn}} + M_{\text{Se}}} \right)^2 \Gamma(\text{Sn}) \right.$$
$$\left. + \left(\frac{M_{\text{Se}}}{M_{\text{Sn}} + M_{\text{Se}}} \right)^2 \Gamma(\text{Se}) \right], \qquad \text{(A5)}$$

where M is the average atomic mass of each atom. Using the above equation, the mass fluctuation parameter was estimated to $\Gamma(\text{SnSe}) = 3.882 \times 10^{-4}$. This value was considered in the phonon spectral properties calculation. Similar calculations were done for Bi_2Te_3, with $\Gamma(\text{Bi}_2\text{Te}_3) = 8.3 \times 10^{-5}$.

All these parameters are used in the calculation of phonon lifetimes and thus for Monte Carlo simulations in order to estimate the thermal conductivity of both compounds. It shall be noted that these Γ values only describe isotopic scattering.

[1] M. S. Dresselhaus, G. Chen, M. Y. Tang, R. G. Yang, H. Lee, D. Z. Wang, Z. F. Ren, J.-P. Fleurial, and P. Gogna, New directions for low-dimensional thermoelectric materials, Adv. Mater. **19**, 1043 (2007).

[2] X. Tang, W. Xie, H. Li, W. Zhao, and Q. Zhang, Preparation and thermoelectric transport properties of high-performance *p*-type Bi_2Te_3 with layered nanostructure, Appl. Phys. Lett. **90**, 012102 (2007).

[3] B. Poudel, Q. Hao, Y. Ma, Y. Lan, A. Minnich, B. Yu, X. Yan, D. Wang, A. Muto, D. Vashaee, X. Chen, J. Liu, M. S. Dresselhaus, G. Chen, and Z. Ren, High-thermoelectric performance of nanostructured bismuth antimony telluride bulk alloys, Science **320**, 634 (2008).

[4] G. Chen, Nanoscale heat transfer and nanostructured thermoelectrics, IEEE Trans. Compon. Packag. Technol. **29**, 238 (2006).

[5] D. G. Cahill, W. K. Ford, K. E. Goodson, G. D. Mahan, A. Majumdar, H. J. Maris, R. Merlin, and S. R. Phillpot, Nanoscale thermal transport, J. Appl. Phys. **93**, 793 (2003).

[6] D. G. Cahill, P. V. Braun, G. Chen, D. R. Clarke, S. Fan, K. E. Goodson, P. Keblinski, W. P. King, G. D. Mahan, A. Majumdar, H. J. Maris, S. R. Phillpot, E. Pop, and L. Shi, Nanoscale thermal transport. II. 2003–2012, Appl. Phys. Rev. **1**, 011305 (2014).

[7] A. Seko, A. Togo, H. Hayashi, K. Tsuda, L. Chaput, and I. Tanaka, Prediction of Low-Thermal-Conductivity Compounds with First-Principles Anharmonic Lattice-Dynamics Calculations and Bayesian Optimization, Phys. Rev. Lett. **115**, 205901 (2015).

[8] B.-L. Huang and M. Kaviany, *Ab initio* and molecular dynamics predictions for electron and phonon transport in bismuth telluride, Phys. Rev. B **77**, 125209 (2008).

[9] O. Hellman and D. A. Broido, Phonon thermal transport in $\text{Bi}_2\text{Te}_3$3 from first principles, Phys. Rev. B **90**, 134309 (2014).

[10] B. Qiu and X. Ruan, Molecular dynamics simulation of lattice thermal conductivity of bismuth telluride using two-body interatomic potentials, Phys. Rev. B **80**, 165203 (2009).

[11] K. Termentzidis, O. Pokropyvnyy, M. Woda, S. Xiong, Y. Chumakov, P. Cortona, and S. Volz, Large thermal conductivity in point defective Bi_2Te_3 bulk materials and superlattices, J. Appl. Phys. **135**, 013506 (2013).

[12] B. Huang, P. Zhai, X. Yang, and G. Li, Effects of mass fluctuation on thermal transport properties in bulk Bi_2Te_3, J. Electron. Mater. **46**, 2797 (2017).

[13] C. X. Yu, G. Zhang, L.-M. Peng, W. Duan, and Y.-W. Zhang, Thermal transport along Bi_2Te_3 insulator nanowires, Appl. Phys. Lett. **105**, 023903 (2014).

[14] S. Li, L. Chaput, N. Stein, C. Frantz, D. Lacroix, and K. Termentzidis, Thermal conductivity of Bi_2Te_3 tilted nanowires, a molecular dynamics study, Appl. Phys. Lett. **106**, 233108 (2015).

[15] C. Shao and H. Bao, Thermal transport in bismuth telluride quintuple layer: Mode-resolved phonon properties and substrate effects, Nat. Sci. Rep. **6**, 27492 (2016).

[16] J. Callaway, Model for Lattice Thermal Conductivity at Low Temperatures, Phys. Rev. **113**, 1046 (1959).

[17] M. G. Holland, Analysis of lattice thermal conductivity, Phys. Rev. **132**, 2461 (1963).

[18] C. J. Glassbrenner and G. A. Slack, Thermal conductivity of silicon and germanium from $3\,^\circ$K to the melting point, Phys. Rev. **134**, A1058 (1964).

[19] C. Jeong, S. Datta, and M. Lundstrom, Full dispersion versus Debye model evaluation of lattice thermal conductivity with a Landauer approach, J. Appl. Phys. **109**, 073718 (2011).

[20] Y. Yang, B. Qiu, A. J. H. McGaughey, X. Ruan, and X. Xu, Mode-wise thermal conductivity of bismuth telluride, J. Heat. Transfer **135**, 091102 (2013).

[21] K. H. Park, M. Mohamed, Z. Aksamija, and U. Ravaioli, Phonon scattering due to van der Waals forces in the lattice thermal conductivity of Bi_2Te_3 thin films, J. Appl. Phys. **117**, 015103 (2015).

[22] M. Munoz Rojo, B. Abad, C. V. Manzano, P. Torres, X. Cartoixa, F. X. Alvarez, and M. Martin Gonzalez, Thermal conductivity of Bi_2Te_3 nanowires: How size affects phonon scattering, Nanoscale **9**, 6741 (2017).

[23] L.-D. Zhao, S.-H. Lo, Y. Zhang, H. Sun, G. Tan, C. Uher, C. Wolverton, V. P. Dravid, and G. Kanatzidis, Ultralow thermal conductivity and high thermoelectric figure of merit in SnSe crystals, Nature (London) **508**, 373 (2014).

[24] J. Carrete, N. Mingo, and S. Curtarolo, Low thermal conductivity and triaxial phononic anisotropy of SnSe, Appl. Phys. Lett. **105**, 101907 (2014).

[25] R. Guo, X. Wang, Y. Kuang, and B. Huang, First-principles study of anisotropic thermoelectric transport properties of IV-VI semiconductor compounds SnSe and SnS, Phys. Rev. B **92**, 115202 (2015).

[26] J. M. Skelton, L. A. Burton, S. C. Parker, A. Walsh, C.-E. Kim, A. Soon, J. Buckeridge, A. A. Sokol, C. R. A. Catlow, A. Togo, and I. Tanaka, Anharmonicity in the High-Temperature *Cmcm* Phase of SnSe: Soft Modes and Three-Phonon Interactions, Phys. Rev. Lett. **117**, 075502 (2016).

[27] H. Yu, S. Dai, and Y. Chen, Enhanced power factor via the control of structural phase transition in SnSe, Nat. Sci. Rep. **6**, 26193 (2016).

[28] R. L. González-Romero, A. Antonelli, and J. J. Melendez, Insights into the thermoelectric properties of SnSe from *ab initio* calculations, Phys. Chem. Chem. Phys. **19**, 12804 (2017).

[29] D. Ibrahim, J.-B. Vaney, S. Sassi, C. Candolfi, V. Ohorodniichuk, P. Levinsky, C. Semprimoschnig, A. Dauscher, and B. Lenoir, Reinvestigation of the thermal properties of single-crystalline SnSe, Appl. Phys. Lett. **110**, 032103 (2017).

[30] S. Wang, S. Hui, K. Peng, T. P. Bailey, W. Liu, Y. Yan, X. Zhou, X. Tang, and C. Uher, Low temperature thermoelectric properties of *p*-type doped single-crystalline SnSe, Appl. Phys. Lett. **112**, 142102 (2018).

[31] P.-C. Wei, S. Bhattacharya, J. He, S. Neeleshwar, R. Podila, Y. Y. Chen, and A. M. Rao, The intrinsic thermal conductivity of SnSe, Nature (London) **539**, E1 (2016).

[32] X. Chen, D. Parker, and D. J. Singh, Acoustic impedance and interface phonon scattering in Bi$_2$Te$_3$ and other semiconducting materials, Phys. Rev. B **87**, 045317 (2013).

[33] U. Aseginolaza, R. Bianco, L. Monacelli, L. Paulatto, M. Calandra, F. Mauri, A. Bergara, and I. Errea, Phonon Collapse and Second-Order Phase Transition in Thermoelectric SnSe, Phys. Rev. Lett. **122**, 075901 (2019).

[34] J. O. Jenkins, J. A. Rayne, and R. W. Ure, Jr., Elastic moduli and phonon properties of Bi$_2$Te$_3$, Phys. Rev. B **5**, 3171 (1972).

[35] W. Kullmann, G. Eichhorn, H. Rauh, R. Geick, G. Eckold, and U. Steigenberger, Lattice dynamics and phonon dispersion in the narrow gap semiconductor Bi$_2$Te$_3$ with sandwich structure, Phys. Status Solidi B **162**, 125 (1990).

[36] D. Bessas, I. Sergueev, H.-C. Wille, J. Perßon, D. Ebling, and R. P. Hermann, Acoustic impedance and interface phonon scattering in Bi$_2$Te$_3$ and other semiconducting materials, Phys. Rev. B **86**, 224301 (2012).

[37] Z.-G. Chen, X. Shi, L.-D. Zhao, and J. Zou, High-performance SnSe thermoelectric materials: Progress and future challenge, Prog. Mater. Sci. **97**, 283 (2018).

[38] K. Peng, X. Lu, H. Zhan, S. Hui, X. Tang, G. Wang, J. Dai, C. Uher, G. Wang, and X. Zhou, Broad temperature plateau for high *ZT*s in heavily doped p-type SnSe single crystals, Energy Environ. Sci. **9**, 454 (2016).

[39] D. Bansal, J. Hong, C. W. Li, A. F. May, W. Porter, M. Y. Hu, D. L. Abernathy, and O. Delaire, Phonon anharmonicity and negative thermal expansion in SnSe, Phys. Rev. B **94**, 054307 (2016).

[40] C. W. Li, J. Hong, A. F. May, D. Bansal, S. Chi, T. Hong, G. Ehlers, and O. Delaire, Orbitally driven giant phonon anharmonicity in SnSe, Nat. Phys. **11**, 1063 (2015).

[41] D. T. Morelli, J. P. Heremans, and G. A. Slack, Estimation of the isotope effect on the lattice thermal conductivity of group IV and group III-V semiconductors, Phys. Rev. B **66**, 195304 (2002).

[42] G. A. Slack and S. Galginaitis, Thermal conductivity and phonon scattering by magnetic impurities in CdTe, Phys. Rev. **133**, A253 (1964).

[43] Y.-J. Han and P. G. Klemens, Anharmonic thermal resistivity of dielectric crystals at low temperatures, Phys. Rev. B **48**, 6033 (1993).

[44] M. Asen-Palmer, K. Bartkowski, E. Gmelin, M. Cardona, A. P. Zhernov, A. V. Inyushkin, A. Taldenkov, V. I. Ozhogin, K. M. Itoh, and E. E. Haller, Thermal conductivity of germanium crystals with different isotopic compositions, Phys. Rev. B **56**, 9431 (1997).

[45] J. W. Schwartz and C. T. Walker, Thermal Conductivity of Some Alkali Halides Containing Divalent Impurities. II. Precipitate Scattering, Phys. Rev. **155**, 969 (1967).

[46] C. Dames and G. Chen, Theoretical phonon thermal conductivity of Si/Ge superlattice nanowires, J. Appl. Phys. **95**, 682 (2004).

[47] R. Prasher, Acoustic mismatch model for thermal contact resistance of van der Waals contacts, Appl. Phys. Lett. **94**, 041905 (2009).

[48] T. Chattopadhyay, J. Pannetier, and H. G. Von Schnering, Neutron diffraction study of the structural phase transition in SnS and SnSe, J. Phys. Chem. Solids **47**, 879 (1986).

[49] https://lammps.sandia.gov/.

[50] https://www.scd.stfc.ac.uk/Pages/DL_POLY.aspx.

[51] D. Lacroix, K. Joulain, and Denis Lemonnier, Monte Carlo transient phonon transport in silicon and germanium at nanoscales, Phys. Rev. B **72**, 064305 (2005).

[52] X. Zianni, V. Jean, K. Termentzidis, and D. Lacroix, Scaling behavior of the thermal conductivity of width-modulated nanowires and nanofilms for heat transfer control at the nanoscale, Nanotechnology **25**, 465402 (2014).

[53] J.-P. M. Péraud and N. G. Hadjiconstantinou, Efficient simulation of multidimensional phonon transport using energy-based variance-reduced Monte Carlo formulations, Phys. Rev. B **84**, 205331 (2011).

[54] H. J. Goldsmid, The thermal conductivity of bismuth telluride, Proc. Phys. Soc., London, Sect. B **69**, 203 (1956).

[55] C. B. Satterthwaite and R. W. Ure, Jr., Electrical and thermal properties of Bi$_2$Te$_3$, Phys. Rev. **108**, 1164 (1957).

[56] H. Kaibe, Y. Tanaka, M. Sakata, and I. Nishida, Anisotropic galvanomagnetic and thermoelectric properties of n-type Bi$_2$Te$_3$ single crystal with the composition of a useful thermoelectric cooling material, J. Phys. Chem. Solids **50**, 945 (1989).

[57] Y. Liu, M. Zhou, and J. He, Towards higher thermoelectric performance of Bi$_2$Te$_3$ via defect engineering, Scr. Mater. **111**, 39 (2016).

[58] H. J. Goldsmid, Recent studies of bismuth telluride and its alloys, J. Appl. Phys. **32**, 2198 (1961).

[59] P.-C. Wei, S. Bhattacharya, Y.-F. Liu, F. Liu, J. He, Y.-H. Tung, C.-C. Yang, C.-R. Hsing, D.-L. Nguyen, C.-M. Wei, M.-Y. Chou, Y.-C. Lai, T.-L. Hung, S.-Y. Guan, C.-S. Chang, H.-J. Wu, C.-H. Lee, W.-H. Li, R. P. Hermann, Y.-Y. Chen, and A. M. Rao, Thermoelectric figure-of-merit of fully dense single-crystalline SnSe, ACS Omega **4**, 5442 (2019).

[60] G. Liu, J. Zhou, and H. Wang, Anisotropic thermal expansion of SnSe from first-principles calculations based on Grüneisen's theory, Phys. Chem. Chem. Phys. **19**, 15187 (2017).

[61] Y. X. C. Chang, Y. Pei, D. Wu, K. Peng, X. Zhou, S. Gong, J. He, Y. Zhang, Z. Zeng, and L.-D. Zhao, Origin of low thermal conductivity in SnSe, Phys. Rev. B **94**, 125203 (2016).

[62] M. Takashiri, K. Miyazaki, S. Tanaka, J. Kurosaki, D. Nagai, and H. Tsukamoto. Effect of grain size on thermoelectric properties of *n*-type nanocrystalline bismuth-telluride based thin films, J. Appl. Phys. **104**, 084302 (2008).

[63] H. Obara, S. Higomo, M. Ohta, A. Yamamoto, K. Ueno, and T. Iida, Thermoelectric properties of Bi_2Te_3-based thin films with fine grains fabricated by pulsed laser deposition, Jpn. J. Appl. Phys. **48**, 085506 (2009).

[64] J. A. Hernandez, A. Ruiz, L. F. Fonseca, M. T. Pettes, M. Jose-Yacaman, and A. Benitez, Thermoelectric properties of SnSe nanowires with different diameters, Nat. Sci. Rep. **8**, 11966 (2018).

[65] D. S. Sanditov and V. N. Belomestnykho, Relation between the parameters of the elasticity theory and averaged bulk modulus of solids, Tech. Phys. **56**, 1619 (2011).

[66] C. Lamuta, D. Campi, L. Pagnotta, A. Dasadia, A. Cupolillo, and A. Politano, Determination of the mechanical properties of SnSe, a novel layered semiconductor, J. Phys. Chem. Solids Phys. **116**, 306 (2018).